Influence of operating temperature on $Li_2ZnTi_3O_8$ anode performance and high-rate charging activity of Li-ion battery

Akbar I. Inamdar,[a] Abu Talha Aqueel Ahmed,[a] Harish S. Chavan,[a] Yongcheol Jo,[a] Sangeun Cho,[a] Jongmin Kim,[a] Sambhaji M. Pawar,[a] Bo Hou,[b] SeungNam Cha,[b] Hyungsang Kim*,[a] Hyunsik Im*,[a]*

[a]Division of Physics and Semiconductor Science, Dongguk University, Seoul 04620, South Korea

[b]Department of Engineering Science, University of Oxford, Parks Road, OX1 3PJ, UK

ABSTRACT: $Li_2ZnTi_3O_8$ (LZTO) is synthesized as an anode material using a facile solid-state-reaction method, and its electrochemical storage properties at different temperatures is investigated along with its ultra-fast-charging activity. X-ray diffraction, Raman spectroscopy, and transmission electron microscopy analyses confirm the formation of spinel LZTO. The LZTO anode half-cell LIB delivers the highest reversible first discharge capacity of 181.3 $mAhg^{-1}$ at a current rate of 0.1 Ag^{-1}. The maximum capacity of 106.97 $mAhg^{-1}$ is obtained within 44 seconds when the LZTO battery is charged at an ultrafast charging rate of 10.0 Ag^{-1}. It shows superior high-rate long-cycle-life stability even at an ultra-high-charging rate, revealing a capacity retention of 106.28% after 100 cycles. The sustainability of the LZTO battery at different temperatures is investigated, and the best results are obtained in a temperature range of 10-40 ^0C with a capacity variation of about 30%. The electrochemical analyses reveal that the LZTO anode exhibits a capacitive-type storage mechanism at high scan rates. The superior fast

charging performance of the LZTO anode is associated with its spinel structure, which forms tunnel-like pathways for easy Li ion diffusion.

KEYWORDS: *$Li_2ZnTi_3O_8$ Anode, ultrafast rechargeable charging, Li ion battery*

Corresponding Author

*E-mail: akbarphysics2002@gmail.com, hskim@dongguk.edu, hyunsik7@dongguk.edu

1. Introduction

As high-performance batteries become essential in various industries and everyday life, great efforts have been made to enhance the battery performance features, such as power density, energy density, cycle life, cost-effectiveness, and charging time, without sacrificing the safety of the battery [1-4]. Among various battery technologies, Li-ion batteries (LIBs) are currently prevalent because of their outstanding advantages, such as higher power density, higher energy density, and longer cycle life compared with other rechargeable batteries. Nowadays there has been an enormous demand for high energy density batteries with fast charging ability for electric vehicles. However, before LIBs can be used in electric vehicles, greater challenges must be overcome: higher energy density and enhanced reaction kinetics for fast charging, thermal stability and high rate operation [5]. Because it takes much longer to charge a battery than to fill a tank with fuel, ultrafast charging may be the answer to wide use of LIBs in electric vehicles. Some studies have found that the synthesis of active nanomaterials and the incorporation of carbon into them improved the charging rate by reducing the diffusion distance and internal resistance [6,7]. In addition, a small modification of the active materials by doping with any

other element could have the same effect in improving the charging rate by reducing the diffusion length. Ultrafast charging may add a stress to the battery, increasing the battery temperature. However, it is suggested that a battery can be charged ultra-fast up to 50% of its capacity and can be moderately charged up to the other half.

Because of good safety and an excellent cycling stability, titanium (Ti)-based complex materials have been synthesized and investigated as a potential LIB anode. For the last two decades, $Li_4Ti_5O_{12}$ (LTO) has been vigorously investigated due to its demonstration of excellent cycling stability [8-12]. but its low theoretical capacity of 175 $mAhg^{-1}$, poor electric conductivity, and high intercalation potential of 1.5 V result in a reduction of the energy density [13, 114]. On the other hand, the Ti-based complex metal oxides, such as LZTO, have been investigated for LIBs, and they have demonstrated a large capacity and sound cycling stability [13, 14, 15]. The Li and zinc (Zn) atoms in the $Li_2ZnTi_3O_8$ structure are located in the tetrahedral sites that form a tunnel-like pathway for an easy Li-ion insertion process. The theoretical LZTO-structure capacity of 227 $mAhg^{-1}$ is higher than that of lithium titanate ($Li_4Ti_5O_{12}$) and its discharge voltage of 0.5 V is lower than that of the Li/Li^+ couple.[15,16] M-doped $Li_2ZnTi_3O_8$ compounds, where M is silver (Ag), aluminum (Al), copper (Cu), nickel (Ni) and C, have also been investigated to effectively improve electrochemical performance by enhancing electronic conductivity and Li-ion diffusivity [17-21]. So far, the testing of $Li_2ZnTi_3O_8$ based LIB anodes has included the following synthetic strategies: (i) preparation of nano-sized particles, (ii) metal-ion doping and (iii) coating with conductive materials. Moreover, the electrochemical performance, cycle life, and safety of the LIBs are affected by the operation or storage temperatures. Fast lithiation/delithiation is one of the most important electrochemical properties of LIBs for high-power applications. The current reports on the LZTO LIB, however, only deal

with its operation at room temperature, and its ultrafast-charging activity has not yet been studied.

In this study, LZTO was synthesized as an LIB anode material via a solid-state-reaction method, and its battery performance was tested at different temperatures ranging from −5 to 55 ^{0}C. The measured maximum-charge storage capacity at a rate of 0.1 Ag^{-1} was ~181 $mAhg^{-1}$ at 25 ^{0}C and ~ 227 $mAhg^{-1}$ at 40 ^{0}C tolerate the ultra-high-charging rates of 1.0, and 10.0 Ag^{-1} delivering the specific capacities of ~ 150 and ~ 107 $mAhg^{-1}$.

2. Experimental

2.1. Material Preparation

The LZTO anode material was prepared using a solid-state-reaction method for which lithium carbonate (Li_2CO_3), zinc oxide (ZnO), and titanium dioxide (TiO_2) served as the raw materials. These three precursor materials were mixed at a molar ratio of 2:1:3 and were ground for 3 hr using an agate mortar. The 5 % extra lithium carbonate was used in order to compensate lithia loss during synthesis process. The powder was then heated in a muffle furnace at 700 ^{0}C for 12 hr in air before it was cooled to room temperature. The obtained product was again ground for 30 min and heated at 900 ^{0}C for 12 hr in air; then it cooled down naturally to room temperature. The final product was filtered using a sheave with a 45-μm pore size to remove the unevenly sized particles.

2.2. Characterization

The crystallinity of the prepared sample was characterized using X-ray powder diffraction (XRD) spectroscopy (with PANalytical's X'pert PRO system, The Netherlands) with Cu Kα

radiation (wavelength λ = 1.54056 Å). Micro (μ)-Raman spectroscopy was performed at room temperature using an argon-ion (Ar^{+}) laser with an excitation wavelength of 532 nm. The structural properties of the sample were investigated using transmission electron microscopy (TEM) (JEM 2010, JEOL Ltd., Japan) with an energy dispersive X-ray (EDX) detector (Oxford Instruments, U.K), high-resolution transmission electron microscopy (HR-TEM), and selected area electron diffraction (SAED). The acceleration voltage and the camera length were 300 kV and 255.8 mm, respectively. The electrochemical properties of the LZTO anode were studied using cyclic voltammetry (CV), galvanostatic charge-discharge, and alternating–current (ac) impedance analysis for which the (MPG-2) battery cycler (Bio-Logic Science Instruments, France) was employed. Temperature-dependent battery performance measurement was performed in a specially designed oven within an error of ± 0.1°.

2.3. Battery fabrication

The battery performance of the LZTO anode was investigated using a CR2032-type coin-cell assembly. The slurry was prepared using $Li_2ZnTi_3O_8$ (80%), carbon black (10%), and a binder (10% polyvinylidene fluoride in N-methyl-2-pyrrolidone). The LZTO anode electrode was uniformly coated on Cu foil using a doctor-blade technique. A half-cell was assembled in an argon (Ar)-filled glove-box using an LZTO disk (15 mm) as a working electrode and Li metal as the counter electrode. A 1M $LiPF_6$ solution that was dissolved in a mixture of ethylene carbonate and dimethyl carbonate with a 1:1 volume ratio was used as the electrolyte.

3. Results and discussion

3.1. Structural and microstructural analysis

The XRD pattern of the LZTO sample is shown in Fig. 1 (a). The main diffraction peaks appear at 30.16°, 35.45°, 43.25°, 56.89°, and 62.53°, and these correspond to the (220), (113), (004), (115), and (404) planes of the cubic-spinel structure of LZTO (JCPDS-44-1037), respectively [13, 14, 15]. Moreover, although some of the minor impurity peaks that are associated with rutile titanium dioxide (TiO_2) were also detected at 27.46°, and 54.36°, their contribution was very small compared with that of the LZTO. The crystal structure of LZTO is described as $(Li_{0.5}Zn_{0.5})^{tet}[Li_{0.5}Ti_{1.5}]^{oct}O_4$ [13, 14, 22]. Thus, the Zn and Li:Ti (1:3) atoms are placed in the tetrahedral and octahedral sites, respectively. The Li and Zn atoms that are located in the tetrahedral sites form a three-dimensional tunnel-like network that is beneficial for Li-ion (Li^+) intercalation [15, 16]. Figure 1(b) shows the Raman spectrum of the LZTO sample. The Raman peaks at 403 and 439 cm^{-1} correspond to the Zn-O and Li-O stretching modes of vibration of ZnO_4 and LiO_4 tetrahedra, respectively. The higher-frequency peak at 716 cm^{-1} is associated with the Ti-O symmetric stretching vibration of the TiO_6 octahedral group [18]. The other peaks are associated with the stretching modes of cation-O bonds and the bending of O-cation-O (below 350 cm^{-1}). The XRD and Raman analyses were consistent, revealing the formation of a high-quality LZTO film.

A scanning-electron-microscopy (SEM) image of the LZTO sample is shown in Fig. 1 (c). The LZTO sample has a granular morphology with different grain sizes. The constituent elements of the LZTO sample were determined using energy dispersive X-ray spectroscopy (EDX), as shown in Fig. 1 (d). The inset of Fig. 1 (d) shows the relative atomic ratios of the

major constituent elements: Zn, Ti, and O. The chemical composition of the LZTO film is $Li_xTi_{3.7}ZnO_{9.6}$.

The LZTO powder was further subjected to the TEM, HR-TEM and SAED studies to assess its microstructural properties and to conduct a qualitative phase analysis. Figure 2 shows the TEM, HRTEM and SAED analyses of the LZTO powder. The large-scale TEM images shown in Figs. 2 (a) and (b) confirm its granular micro-size morphology, and this is consistent with the SEM image in Fig. 1(c). Clear lattice-fringe regions are observed in the HR-TEM image (Figs. 1(c)), revealing its good crystallinity. The lattice distances of the (113), (220), and (110) planes (d_{113}, d_{220}, d_{110}) of the selected area (marked with a box in Fig. 2 (d)) are 2.50 ± 0.1 Å, 2.92 ± 0.1 Å, and 5.9 ± 0.1 Å, respectively (Fig. 2 (e)). The observed lattice distances match well with the standard lattice distances of the cubic-LZTO structure [15]. Figure 1(f) shows a typical SAED pattern, which can be readily indexed to the LZTO lattice configuration [22]. The images of the moire fringes are shown in Fig. S1 (Supporting Information). The presence of mixed moire fringes, including translation and rotation, indicates the layered features of the prepared LZTO material [23].

3.2. Cyclic voltammetry

Figure 3(a) shows the first three CV curves of the LZTO electrode in the half-cell configuration at room temperature. The electrochemical behavior of the first cycle is different from that of the subsequent cycles, and this is because of the polarization of either the cell or the local structural changes [24]. The CV curves show a pair of cathodic (1.22 V vs. LI/Li^+) and anodic (1.83 V vs. LI/Li^+) peaks that are associated with the phase transition between the spinel and the rock salt [14]. The anodic peak shifts toward a higher positive potential with an

increasing number of cycles, while the cathodic peak remains unchanged. An additional reduction peak around 0.5 V (vs. Li/Li^+) corresponds to the multiple restorations of the Ti^{4+} ions [24-26]. During the anodic sweep, the peak around 2.5 V (vs. Li/Li^+) is likely due to the decomposition of the amorphous lithium oxide (Li_2O) [22].

3.3 Galvanostatic charge-discharge properties

A comprehensive understanding of battery performance characteristics at different operating temperatures is important because the LZTO material exhibits different kinetics under different environments. Here, the galvanostatic charge-discharge properties of the LZTO electrode were investigated at different temperatures ranging from –5 to 55 °C. Figure 3(b) shows the first galvanostatic charge-discharge curves that were measured at a current density of 0.1 Ag^{-1} and at various temperatures. The charge-discharge characteristics at different temperatures are similar in shape, suggesting the similarity of the electrochemical reactions. They show voltage plateaus in the range of 0.2 to 0.7 V versus the Li/Li^+ during the lithiation and in the range of 1.4 to 1.7 V versus the Li/Li^+ during delithiation. The voltage plateaus were widened at high temperatures. The difference between the lithiation and delithiation plateaus becomes smaller with increasing temperatures. This voltage plateau temperature-dependent behavior is a result of the kinetic effect of the material. The reduced voltage difference between the lithiation-delithiation plateaus at 55 °C is due to the faster kinetics, and the direct evidence of this is obtained from the temperature-dependent electrochemical impedance-spectroscopy (EIS) data (Fig. S2 in the Supporting Information). The reduced charge-transfer resistance values at higher temperatures indicate the kinetic effect of the material.

The initial discharge-capacity values of the LZTO electrode are 131.2, 131.1, 183.3, 227.3 and 233.1 $mAhg^{-1}$ at –5, 10, 25, 40 and 55 °C, respectively. A similar trend is evident in terms of the charge capacity, as shown in Fig. S3 (Supporting Information). The charge-discharge curves for the first five cycles measured at 25 °C and at 0.1 Ag^{-1} are shown in Fig. S4 (Supporting Information). The initial discharge capacity of 183.3 $mAhg^{-1}$ decreases to 147.1 $mAhg^{-1}$ at the fifth cycle. The comparative temperature-dependent capacity retention of the LZTO electrode is shown in Fig. 3(c). The maximum capacity values are obtained at 40 °C for the charge process and at 55 °C for the discharge process. The capacity variation in the given operating temperature range is within 30%.

3.4. Rate capability and long-cycle electrochemical stability

The LZTO electrode was cycled at various charge-discharge current densities for five cycles to investigate the rate performance. Figure 3(d) shows the cycling-rate performances measured at 25 and 40 °C. The cycling performances measured at the other temperatures of –5, 10, and 55 °C are shown in Fig. S5 (Supporting Information). The initial charge capacity at 0.1 Ag^{-1} is 183.3 $mAhg^{-1}$ at 25 °C and 227.3 $mAhg^{-1}$ at 40 °C, but at 5 Ag^{-1}, it decreases to 23.5 and 16.7 $mAhg^{-1}$, respectively. The initial capacity loss (irreversible capacity) between the first and second discharges of the electrode is likely due to the irreversible decomposition of the electrolyte and the formation of a solid electrolyte interface (SEI) [24, 27]. As the applied current was set back to 1 Ag^{-1}, the specific capacity of the LZTO electrode was recovered to 105% at 25 °C and 111% at 40 °C, and this increased specific capacity might be due to the activation of the electrode after the initial cycling. The LZTO electrode at 25 °C shows an improved rate

capability at various rates compared with the 40 °C test. On the other hand, the LZTO electrode tested at –5, 10, and 55 °C exhibits unstable performances (Fig. S5) at each rate of the applied current density.

The rate performance and the long-cycle electrochemical stability at 25 °C was further tested for up to 500 charge-discharge cycles at a high rate of 1 Ag^{-1}. Figure 4(a) shows the cycling stability and the Coulombic efficiency at 1 Ag^{-1} for 500 charge-discharge cycles. The specific capacity and Coulombic efficiency of the first cycle is 56.83 $mAhg^{-1}$ and 99%, respectively. The overall Coulombic efficiency of the electrode is larger than 98% over the 500 charge-discharge cycles, demonstrating that the sample has good cycling performance and reversibility. The obtained Coulombic efficiency of the LZTO electrode is comparable to that of commercial anodes and is much higher than that of the carbon anode (60%) [28-30]. After the first few cycles, the capacity increases quickly up to 100 charge-discharge cycles, and this is presumably because of the activation of the electrode, the electrolyte decomposition, or the SEI formation [24, 31]. The capacity decreases up to 250 cycles, and it then becomes stable over 500 charge-discharge cycles. The samples have a capacity retention of ~ 64% after the 500 charge-discharge cycles with a capacity fading of only 0.072% per cycle. The observed rolling-cycling performance at a high rate could be due to the formation of a polymeric/gel-like layer during the fast-charging/discharging processes [32].

EIS was performed to quantitatively evaluate the electrochemical behavior of the LZTO electrode before and after the cycling. Figure 4(b) shows the Nyquist plot and the fitting curves (lines). The inset shows the equivalent circuit diagram used for the fitting. The Nyquist plot consists of a semi-circle in the high-frequency region and a straight line in the low-frequency region. The straight line portion is associated with the diffusion of the Li^+ to the electrode. The

Warburg impedance is referred to as W_{01}, R_s is the solution resistance, R_{ct} is the charge-transfer resistance, and the *CPE* is the constant phase element. The fitted impedance parameters are listed in Table I. The pre-cycling initial R_{ct} of the electrode is 135 **Ω**, but it decreases to 57 **Ω** after cycling. The considerably improved post-cycling *Rct* is mainly due to the increase in the electrical conductivity during the lithiation/delithiation and the enhanced electrode-material contact area. The origin of this activation step is the delayed wetting of the electrolyte into the composite electrode [33].

3.5. Fast-charge/slow-discharge characteristics

The LZTO electrode was tested at the fast charging rates of 1.0 and 10.0 Ag^{-1}, and it was discharged at 0.1 Ag^{-1} for 100 consecutive charge-discharge cycles. The typical charge-discharge profile of the LZTO electrode that was charged at 1.0 Ag^{-1} and discharged at 0.1 Ag^{-1} is shown in Fig. 5(a). The shape of the charge profile is similar to that of the voltage profile during the slow-charging process (Fig. 3(b)). Figure 5(b) shows the charging curves of the LZTO electrode at the current densities of 1.0 and 10.0 Ag^{-1}, and Figure 5(c) shows the discharging curves when the electrodes are discharged at 0.1 Ag^{-1}. The shapes of the discharge curves (Fig. 5 (c) charged at 1.0 and 10.0 Ag^{-1}) are very similar to those of the curves that are charged at 0.1 Ag^{-1}, as shown in Fig. 3(b). The results obtained from the fast-charging and slow-discharging experiments are summarized in Table-II. The electrode that is charged at 1.0 Ag^{-1} exhibits the maximum specific capacity of 149.88 $mAhg^{-1}$, but it decreases to 106.97 $mAhg^{-1}$ at 10.0 Ag^{-1}. Figure 5(d) shows the long-term specific discharge capacity and the capacity retention as a function of the number of cycles when the electrode is charged at 1.0 and 10.0 Ag^{-1}. At an ultra-high-charging rate of 10.0 Ag^{-1}, the specific capacity and the capacity retention increases

gradually during the first 50 charge-discharge cycles, and then they decrease over the next 100 charge-discharge cycles. A similar trend is observed when the electrode is charged at 1.0 Ag^{-1}. The maximum capacity of 106.97 $mAhg^{-1}$ at 10.0 Ag^{-1} is achieved with a very short charging time of 44 s (Table-II). The electrode that is charged at 1.0 and 10.0 Ag^{-1} shows excellent capacity-retention values of 96.98 and 106.28%, respectively, demonstrating an excellent electrode sustainability, even at ultra-high-charging rates.

3.6. Capacitive and diffusion-limited contributions

To understand the electrochemical performance, the reaction kinetics of the LZTO electrode was studied using CV at various scan rates ranging from 0.2 to 5.0 mVs^{-1}, as seen in Fig. 6 (a). The observed total capacity is the sum of the capacitive and diffusion-limited contributions. The stronger and broader scan-rate-related cathodic and anodic peaks are characteristic features of the large polarization that occurs at high scan rates [34]. The anodic and cathodic currents (i) obey the power-law relationship with the scan rate (ν) as follows [35]

$$i = a \times \nu^{b} \quad (1)$$

where a and b are the fitting parameters. The kinetics of the Li^{+} intercalation during during the cathodic and anodic are analyzed by plotting the log(i)-log(ν) curves. Figure 6(b) shows the log(i)-log(ν) characteristics. The estimated b (slope) values for the cathodic and anodic currents are 0.68 and 0.71, respectively, indicating that the reaction current is obtained from two phenomena, the intercalation and the surface capacitance. (If the slope is less than 0.5 it is diffusion controlled and if the slope is more than 1 it is capacitive-type storage mechanism). To quantitatively estimate the capacitive and diffusion-controlled contributions, the following equation can be used [34, 35].

$$i = k_1 \times \nu + k_2 \times \nu^{1/2} \quad (2)$$

where k_1 and k_2 are the fitting parameters. The "$k_1 \times \nu$" is the capacitive contribution and "$k_2 \times \nu^{1/2}$" represents the diffusion-controlled contribution. The obtained k_1 and k_2 values are 0.8417 and 0.1823, respectively (Fig. S6 in Supplementary Information). Figure 6(c) shows the capacitive ($k_1 \times \nu$) and diffusion-controlled ($k_2 \times \nu^{1/2}$) contributions in the CV curve measured at 0.2 mV/s. Figure 6(d) shows the calculated contribution ratio between the capacitive and diffusion-controlled portions, as a function of scan rate ν. As anticipated, the capacitive contribution increases linearly with an increasing scan rate, but the opposite is true for the diffusion-controlled contribution.

4. Conclusion

We successfully synthesized LZTO via a solid-state-reaction method and investigated the material as an anode electrode for LIB applications. The LZTO electrode exhibited high reversible-capacity values of 181.3 $mAhg^{-1}$ at 25 °C and 227.3 $mAhg^{-1}$ at 40 °C, rate performance, and sound kinetic characteristics at different operating temperatures. The electrode exhibited good sustainable electrochemical behavior at different operating temperatures. The LZTO electrode had a good capacity retention of 64% after 500 charge-discharge cycles with a capacity fading of only 0.072% per cycle. An excellent Coulombic efficiency larger than 98% was obtained; this value is comparable to those of the commercially available anodes and much higher than those of carbon-based anodes such as graphite (60%). The LZTO anode delivered a 106.97 $mAhg^{-1}$ capacity when it was charged at an ultra-fast rate of 10.0 Ag^{-1} with a very short charging time of 44 s.

Acknowledgments

This project was supported by the National Research Foundation (NRF) of Korea (Grant nos. 2015R1D1A1A01058851, 2018R1A2B6007436, 2016R1A6A1A03012877, and 2015R1D1A1A01060743).

References

[1] X. Chen, S. Wang, H. Wang, Electrochimica Acta 265 (2018) 175-183.

[2] Z. Wanga, P. Fei, H. Xiong, C. Qin, W. Zhao, X. Liu, Electrochimica Acta 252 (2017) 295–305.

[3] X. Liu, D. Wang, B. Zhang, C. Luan, T. Qin, W. Zhang, D. Wang, X. Shi, T. Deng, W. Zheng, Electrochimica Acta 268 (2018) 234-240.

[4] H. L. Tsai, C. T. Hsieh, J. Li, Y. A. Gandomi, Electrochimica Acta 273 (2018) 200-207.

[5] I. H. Son, J. H. Park, S. Park, K. Park, S. Han, J. Shin, S. G. Doo, Y. Hwang, H. Chang & J. Wook, Nat. Comm. 8 (2017) 1561.

[6] H. Kim, M.G. Kim, H.Y. Jeong, H. Nam, J. Cho, Nano Lett. 15 (2015) 2111-2119.

[7] S. Wu, R. Xu, M. Lu, R. Ge, J. locozzia, C. Han, B. Jiang and Z. Lin, Adv. Energy Mater. 5 (2015) 1500400.

[8] N. Li, J. Liang, D. Wei, Y. Zhu, Y. Qian, Electrochimica Acta 123 (2014) 346–352.

[9] Z Lin, Y. Yang, J. Jin, L. Wei, W. Chen, Y. Lin, Z. Huang, Electrochimica Acta 254 (2017) 287–298.

[10] H. Xu, X. Hu, Y. Sun, W. Luo, C. Chen, Y. Liu, Y. Huang, Nano Energy 10 (2014) 163–171.

[11] Q. Xia, N. Jabeen, S. V. Savilov, S. M. Aldoshin, H. Xia, J. Mater. Chem., A 4 (2016) 17543-17551.

[12] C. Wang, S. Wang, L. Tang, Y. B. He, L. Gan, J. Li, H. Du, B. Li, Z. Lin, F. Kang, nano energy 21 (2016) 133-144.

[13] Z. Hong, M.Wei, X. Ding, L. Jiang, K. Wei, Electrochem. Commun. 12 (2010) 720-723.

[14] T. Liu, H. Q. Tang, L.X. Zanc, Z.Y. Tang, J. Electroanal. Chem. 771 (2016) 10-16.

[15] L. Wang, L. J. Wu, Z .H. Li, G. T. Lei, Q. Z. Xiao, P. Zhang, Electrochim. Acta 56 (2011) 5343-5346.

[16] Y. X. Xu, Z. S. Hong, L. C. Xia, J. Yang, M. D. Wei, Electrochim. Acta, 88 *(*2013) 74-78.

[17] H. Q. Tang, Z. Y. Tang, C. Q. Du, F. C. Qie, J. T. Zhu, Electrochim. Acta 120 (2014) 187-192.

[18] H. Q. Tang, J. G. Zhu, Z. Y. Tang, C. X. Ma, Journal of Electroanalytical Chemistry, 731 (2014) 60-66.

[19] Y. Li, C. Q. Du, J. Liu, F. Zhang, Q. Xu, D. Qu, X. H. Zhang, Z. Y. Tang, Electrochim. Acta 167 (2015) 201-206.

[20] S. K. Singh, S. R. Kiran, V. R. K. Murthy, Materials Chemistry and Physics 141 (2013) 822-827.

[21] Y. Xu, Z. H. Hong, L. Xia, J. Yang, M. D. Wei, Electrochim. Acta 88 (2013) 74-78.

[22] Z. S. Hong, X. G. Zheng, X. K. Ding, L. L. Jiang, M. G. Wei, K. Wei, Energy Environ. Sci. 4 (2011) 1886-1891.

[23] R. I. Bickley, T. Gonzalezcarreno, J. S. Lees, L. Palmisano, R. J. D. Tilley, J. Solid State Chem. 92 (1991) 178-190.

[24] A. I. Inamdar, R. S. Kalubarme, J. Kim, Y. Jo, H. Woo, S. Cho, S. M. Pawar, C. J. Park, Y. W. Lee, J. I. Sohn, S. Cha, J. Kwak, H. Kim, H. Im, J. Mater. Chem. A, 4 (2016) 4691-4699.

[25] H. Ge, N. Li, D. Li, C. Dai, D. Wang, Electrochem. Commun. 10 (2008) 719-722.

[26] W. J. H. Borghols, M. Wagemaker, U. Lafont, E. M. Kelde, F.M. Mulder, J. Am. Chem. Soc. 131 (2009) 17786-17792.

[27] R. S. Kalubarme, A. I. Inamdar, D. S. Bhange, H. Im, S. W. Gosavi, C. J. Park, J. Mater. Chem. A 4 (2016) 17419-17430.

[28] A. Rudola, K. Saravanan, C. W. Mason and P. Balaya, J. Mater. Chem. A 1 (2013) 2653-2662.

[29] Y. Sun, L. Zhao, H. Pan, X. Lu, L. Gu, Y. S. Hu, H. Li, M. Armand, Y. Ikuhara, L. Chen, X. Huang, Nat. Commun. 4 (2013) 1870.

[30] B. Guo, J. Shu, K. Tang, Y. Bai, Z. Wang, L. Chen, J. Power Sources 177 (2008) 205-210.

[31] Z. Cai, L. Xu, M. Yan, C. Han, L. He, K. M. Hercule, C. Niu, Z. Yuan, W. Xu, L. Qu, K. Zhao and L. Mai, Nano Lett. 15 (2015) 738-744.

[32] X. Jiang, W. Yu, H. Wang, H. Xu, X. Liu, Y. Ding, J. Mater. Chem. A 4 (2016) 920-925.

[33] H. Wu, G. Yu, L. Pan, N. Liu, M. T. McDowell, Z. Bao, Y. Cui, Nat. Commn. 4 (2013) 1943.

[34] Y. Dou, Y. Wang, D. Tian, J. Xu, Z. Zhang, Q. Liu, B. Ruan, J. Ma, Z. Sun, S. X. Dou, 2D Mater. 4 (2017) 015022.

[35] S. Loua, X. Cheng, Y. Zhao, A. Lushington, J. Gao, Q. Li, P. Zuo, B. Wang, Y. Gao, Y. Ma, C. Du, G. Yin, X. Sun, Nano Energy 34 (2017) 15-25.

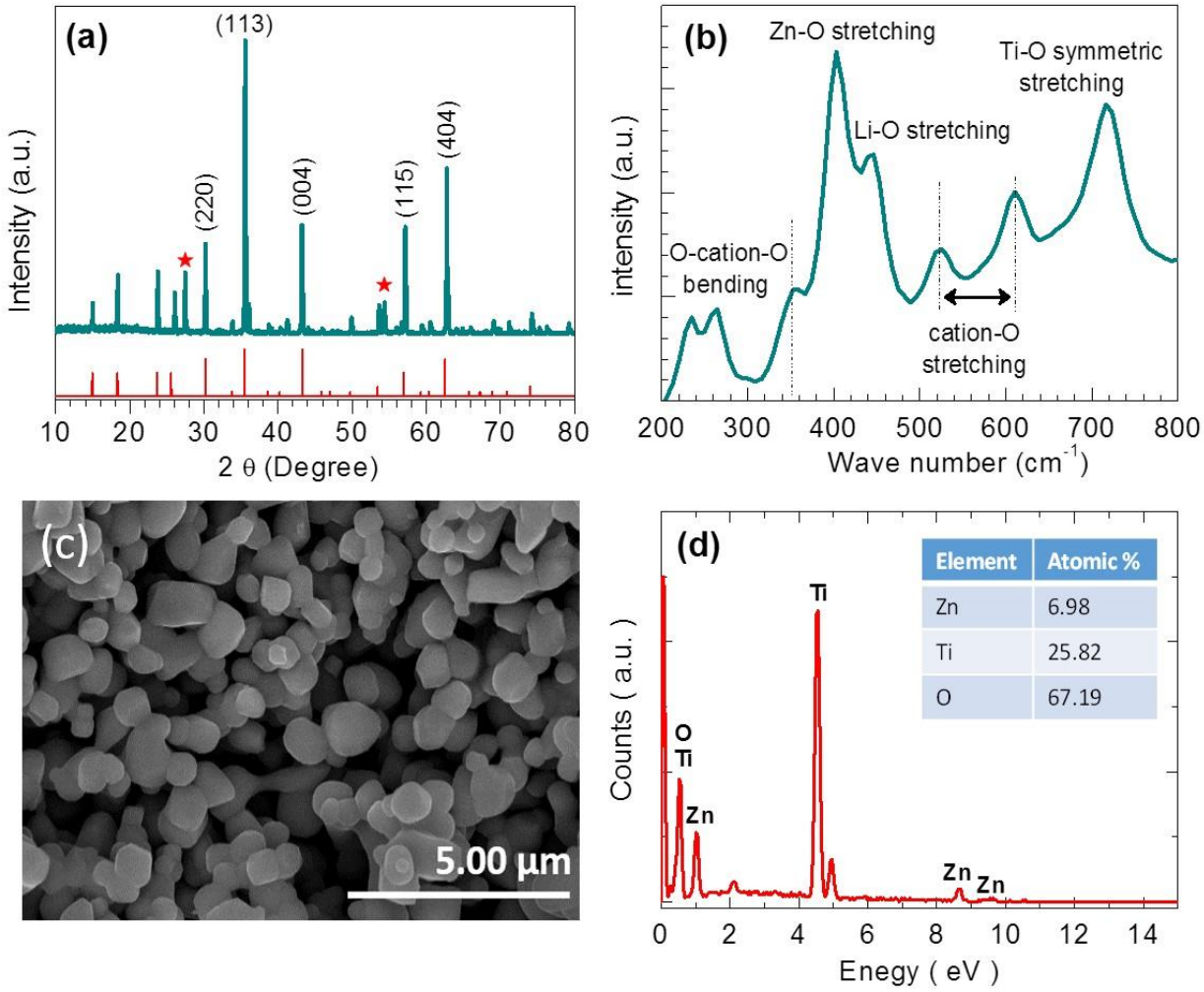

Fig. 1. (a) X-ray-diffraction (XRD) pattern of the $Li_2ZnTi_3O_8$ (LZTO) sample synthesized using a solid-state-reaction method, confirming the formation of the cubic-spinel LZTO structure JCPDS 44-1037. (b) Raman spectrum, (c) SEM image showing that the LZTO has a granular morphology. (d) Energy dispersive X-ray analysis spectra of the LZTO.

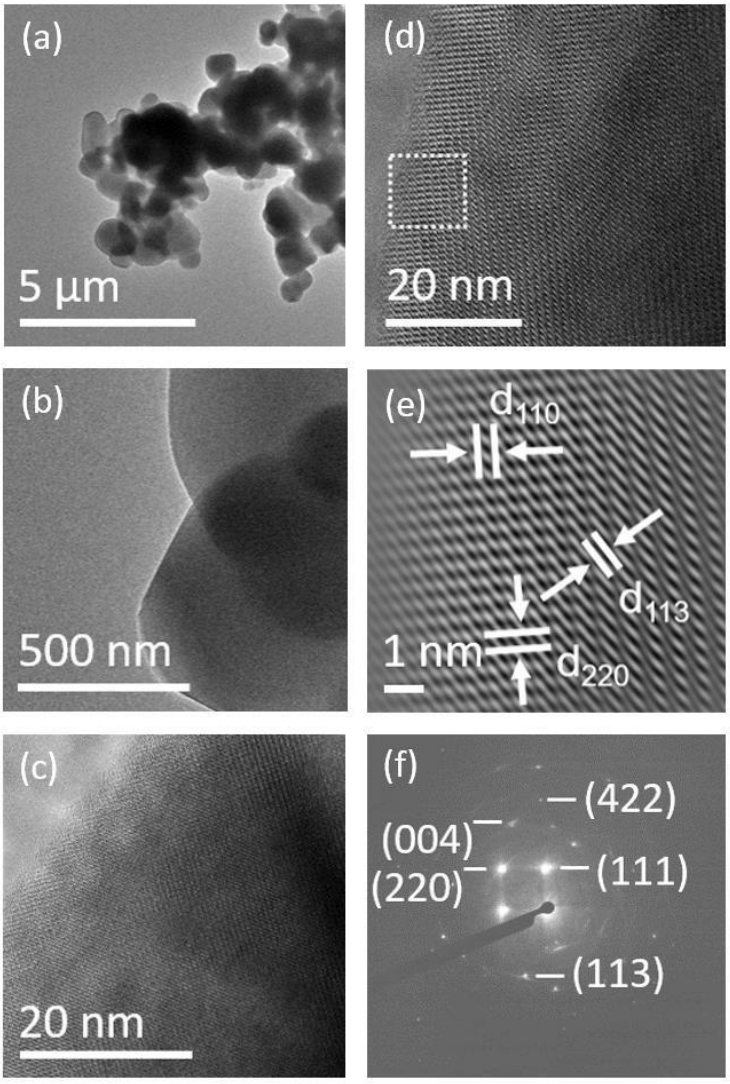

Fig. 2. (a and b) Transmission-electron-microscopy (TEM) and (c) high-resolution transmission-electron-microscopy (HRTEM) images of the LZTO powder. These images reveal that the particles are homogenous and are micro-sized, and the continuous lattice fringes that were detected in the HRTEM image confirmed that the product is in a highly crystalline state; The lattice distances for the selected area in (d) and that are shown the $d_{113,}$ $d_{220,}$ and d_{110} planes in (e) are 2.50 ± 0.1 A, 2.92 ± 0.1 A, and 5.9 ± 0.1 A for the (113), (220), and (110) planes, respectively, (f) The crystallographic planes were obtained from the selected-area-electron-diffraction (SAED) patterns and are associated with the JCPDS 44-1037.

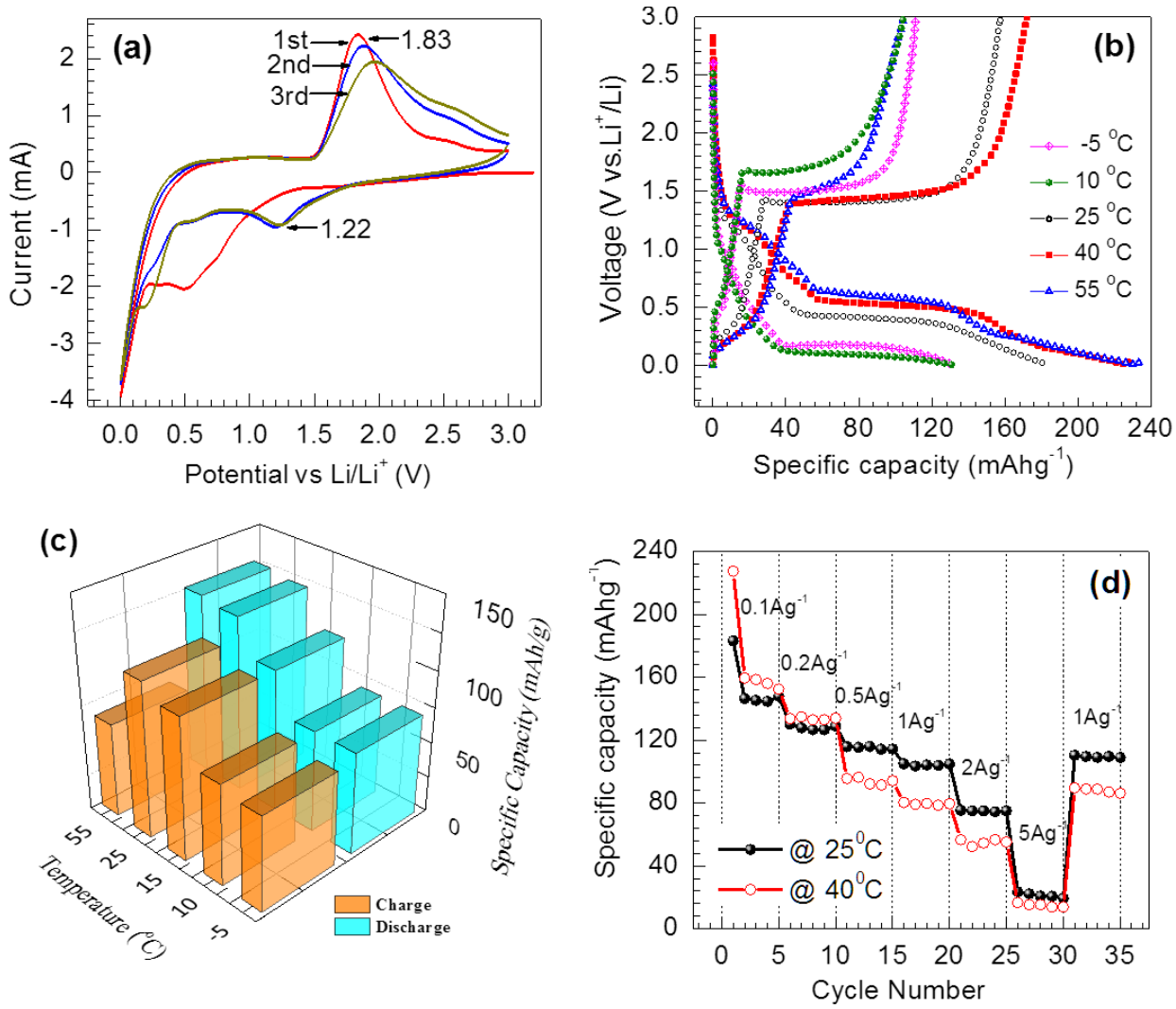

Fig. 3. (a) First three cyclic-voltammetry (CV) curves of the $Li_2ZnTi_3O_8$ (LZTO) electrode in the half-cell configuration measured at an operating temperature of 25 °C. (b) First galvanostatic charge-discharge characteristics of the LZTO measured at different temperatures from –5 to 55 °C. (c) temperature-dependent retention of the charge-discharge capacity of the LZTO electrode. (d) Rate performances of the LZTO electrode.

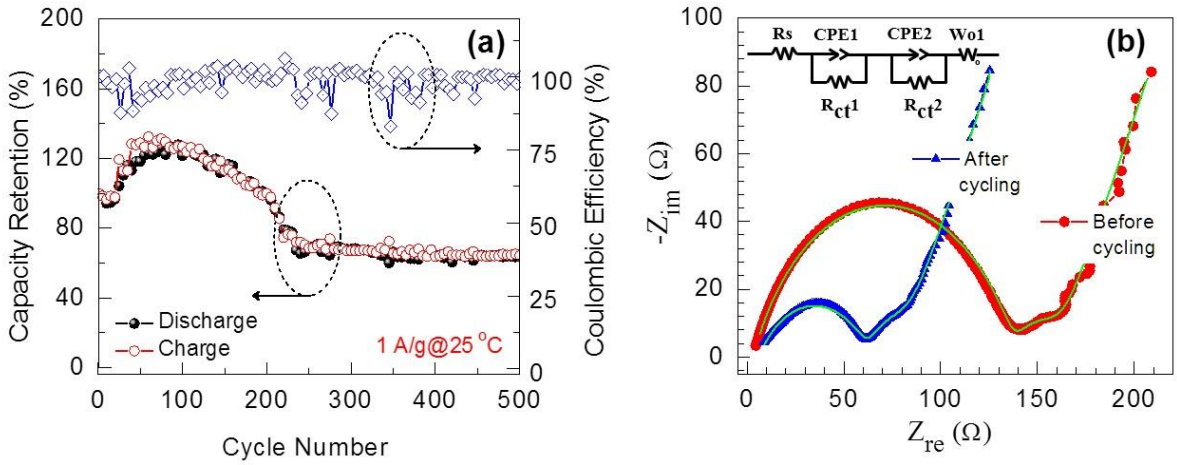

Fig. 4. (a) High-rate long-life-cycling performance and Coulombic efficiency of the LZTO electrode at 25 °C for up to 500 charge-discharge cycles at 1 Ag^{-1}. (b) Nyquist plots before and after the 500th charge-discharge cycling test. The lines represent the fitting curves using the equivalent-circuit diagram (inset).

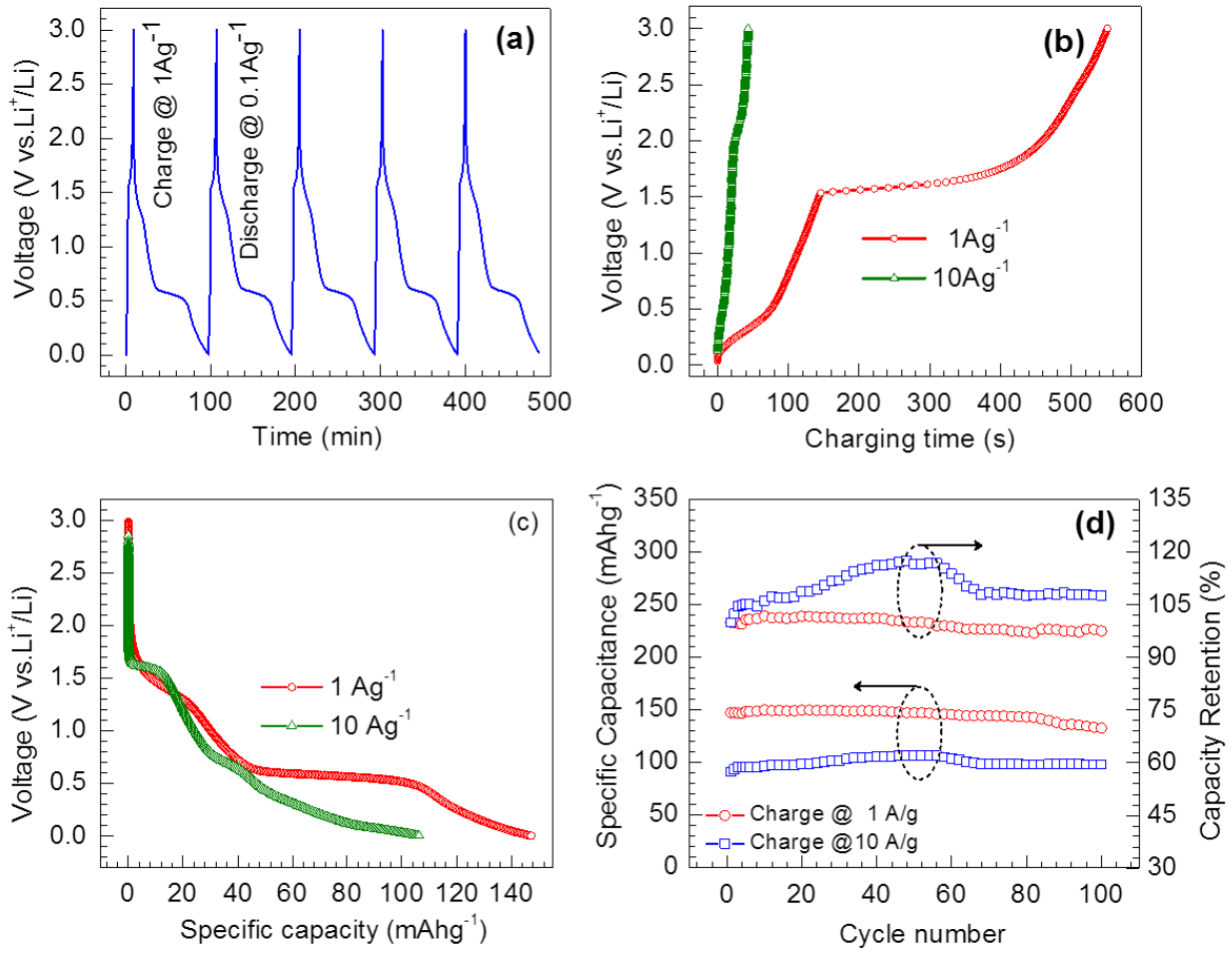

Fig. 5. (a) The typical charge-discharge profile of the $Li_2ZnTi_3O_8$ (LZTO) electrode that was charged at a fast rate of 1.0 Ag^{-1} and discharged at a slow rate of 0.1 Ag^{-1}. (b) Galvanostatic-charge profile of the LZTO electrode at current densities of 1.0, and 10.0 Ag^{-1}. (c) Galvanostatic-discharge (at the rate of 0.1 Ag^{-1}) profile of the LZTO electrode those were charged at 1.0 and 10.0 Ag^{-1}. (d) Specific discharge capacity and the capacity retention as a function of the number of cycles for 100 charge-discharge cycles when the electrodes were charged at the fast rates of 1.0 and 10.0 Ag^{-1}.

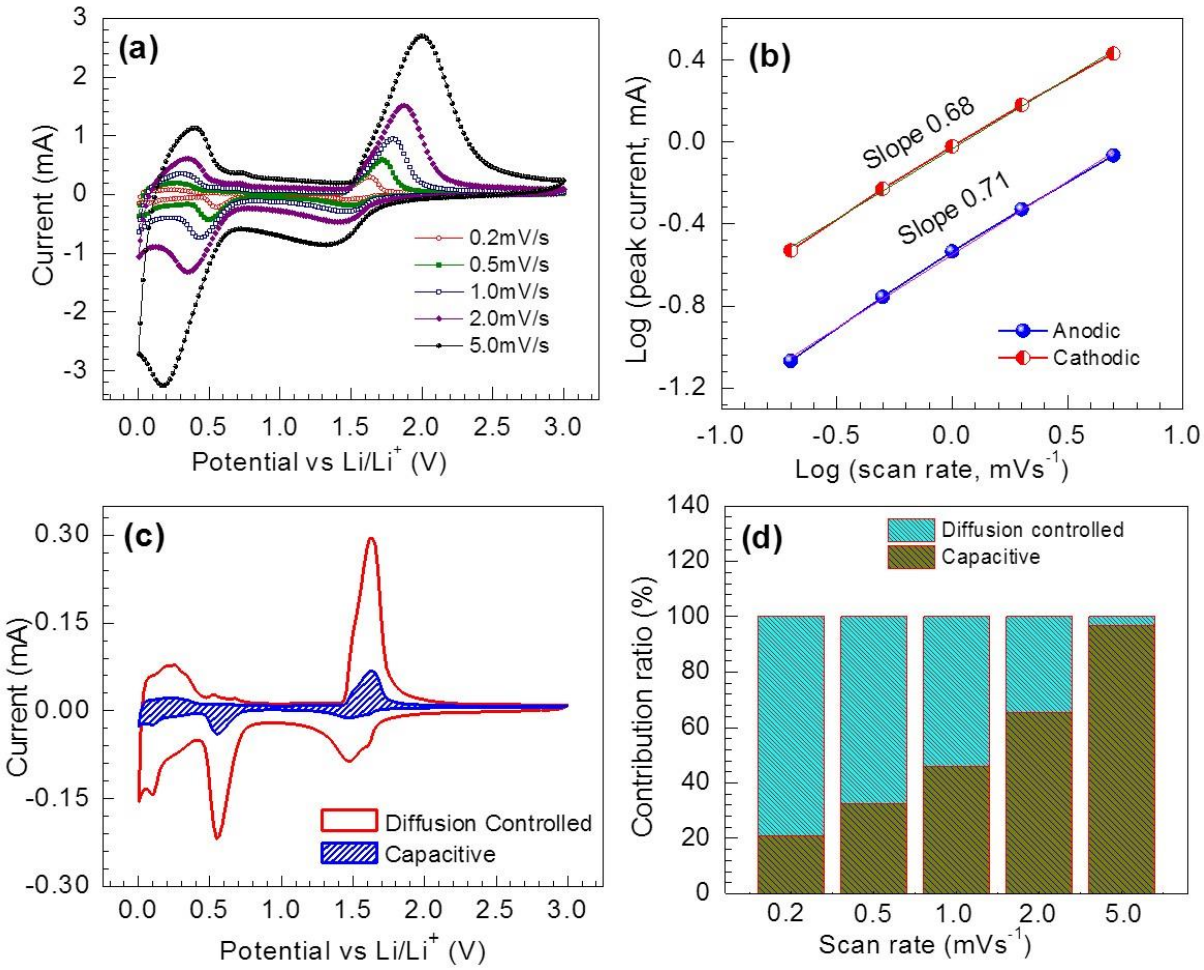

Fig. 6. (a) Cyclic-voltammetry (CV) curves at different scan rates 0.2, 0.5, 1.0, 2.0, and 5.0 mVs^{-1}. (b) The slope of log (*i*) vs log (ν) curves gives the information about the mechanism exhibiting into the electrode. (If the slope is less than 0.5 it is diffusion controlled and if the slope is more than 1 it is controlled by the capacitive-type storage mechanism) (c) Capacitive and diffusion-controlled currents as a function of potential (vs. Li/Li+) at the scan rate of 0.2 mVs^{-1}. (d) Comparison of the capacitive-charge storage and the diffusion-controlled charge storage at different scan rates.

	Before test	After 500 cycles
R_s *(Ω)*	3.25	6.03
R_{ct1} *(Ω)*	135	57
R_{ct2} *(Ω)*	22	13.76
CPE1 (μF)	0.743	0.621
CPE1 (μF)	0.725	0.910

Table I. Impedance parameters of the $Li_2ZnTi_3O_8$ (LZTO) electrode before and after the 500th charge-discharge cycle.

Current density Ag^{-1}	**Charging time (sec)**	**Discharge capacity $mAhg^{-1}$**	**Capacity retention after 100 cycles (%)**
1.0	591	149.88	97.54
10.0	44	106.97	106.28

Table II. Galvanostatic charge-discharge results and capacity retention that were obtained from the fast-charging and slow-discharging experiments.

Table of content

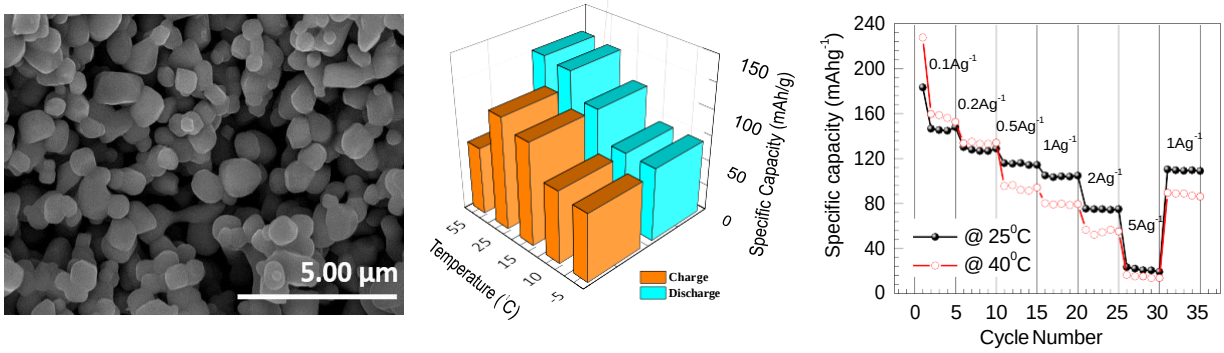

We developed an ultrafast rechargeable $Li_2ZnTi_3O_8$ (LZTO) anode for lithium ion battery application. The half-cell LZTO battery delivers the highest reversible first discharge capacity of 181.3 $mAhg^{-1}$ at a current rate of 0.1 $Ag^{-}1$ (0.1C). The maximum capacity of 106.97 $mAhg^{-1}$ was obtained within 44 seconds when the LZTO battery was charged at an ultrafast charging rate of 10.0 Ag^{-1} (10 C). It showed excellent capacity-retention of 106.28%, suggesting an excellent electrode sustainability, even at ultra-high-charging rates.